Transient hydrodynamics and free surface capture of an under-baffled stirred tank during stopping

Jean-Philippe Torré, D. F. Fletcher, Thierry Lasuye, Catherine Xuereb

TRANSIENT HYDRODYNAMICS AND FREE SURFACE CAPTURE OF AN UNDER-BAFFLED STIRRED TANK DURING STOPPING

J. P. Torré[1,2,*], D. F. Fletcher[2], T. Lasuye[3] and C. Xuereb[1]

[1]Université de Toulouse, Laboratoire de Génie Chimique, CNRS/INP/UPS, Toulouse, France.
[2]School of Chemical and Biomolecular Engineering, The University of Sydney, NSW, Australia.
[3]LVM Quality and Innovation Department, Usine de Mazingarbe, Chemin des Soldats, Bully Les Mines, France.

Abstract: The transient hydrodynamics and the free surface shape have been numerically predicted by CFD for an under-baffled agitated vessel during the stopping phase of the agitator, including the inertial period after the agitator has completely stopped. The simulations were carried out in a fully transient manner using a gas/liquid inhomogeneous two phase flow model coupled with a $k-\varepsilon$ turbulence model. The time dependence of the system studied reveals that the history of the fluid evolution during the impeller slowing phase determines the instantaneous results, implying that the resulting hydrodynamics cannot be determined via a classical steady-state approach. The numerical prediction of the free surface shape during stopping is in agreement with experimental data.

Keywords: agitator stopping; free surface; under-baffled vessel; mixing; CFD; transient simulation.

INTRODUCTION

It is important to be able to calculate the transient hydrodynamics with high accuracy during the stopping phase of a reactor, especially when this stopping is due to a breakdown of the process. In particular, such simulations can be very useful to design and choose operating parameters for injecting an inhibiting solution to stop the chemical reaction quickly. Many chemical reactions within the process industries are exothermic. Generally, the removal of this heat from the reactor is carried out using internal cooling coils, jackets or external heat exchangers. If the rate of heat generation exceeds the rate of heat removal, a self-sustaining uncontrolled runaway reaction may occur. In fact 26.5% of the major accidents in the chemical industries are the result of runaway reactions (Balasubramanian and Louvar, 2002) and an analysis of 189 incidents that occurred in the UK chemical industry between 1962 and 1987 (Barton and Nolan, 1989) revealed that polymerization reactions account for almost 50% of the incidents for which there was a high potential for loss of control and runaway. One of the major reasons for runaway is power failure (Dakshinamoorthy *et al.*, 2006). The safe operation of a stirred vessel in which a runaway reaction could potentially occur is essential, not only for the reactor itself but also for the plant workers and the chemical plant surroundings.

In order to control a runaway reaction, an inhibiting agent (known as a 'killer' or 'stopper' in polymer processes) can be dosed for quenching the reaction (Dakshinamoorthy *et al.*, 2004). As these killers are very active substances, the reaction inhibition process involves the injection of a small quantity of fluid into the reactor, requiring rapid mixing in the bulk and an injection location well adapted to give a high efficiency. The mixing behaviour depends not only on geometric parameters, such as the nozzle type, the reactor and baffles, and the agitator but also on fluid dynamic and physical properties. The mixing of an inhibiting agent in a stirred reactor has already been studied by various workers, e.g., Dakshinamoorthy *et al.* (2004, 2006), Hristov and Mann (2002) or Kammel *et al.* (1996), with an agitator continuously in rotation. A particularly interesting case, which has rarely been studied, is the mixing of the killer (or stopper) during the slow down and stopping phase of the agitator. This situation is frequently encountered when an exothermic reaction is to be quenched following an unplanned power shutdown.

Much published work has studied the transient mixing in a stirred tank, such approaches becoming more feasible due to the improvement of computers. Numerical methods such as direct numerical simulation (DNS) and large eddy simulations (LES) can now be used. DNS resolves all turbulent length and time scales and implies that the numerical grid has to be smaller than the Kolmogorov scale. Verzicco *et al.* (2004), and recently Sbrizzai *et al.* (2006) who coupled DNS with Lagrangian tracking particles, have investigated unbaffled stirred tank reactors. In the LES model, the continuity and momentum equations are filtered prior to being solved in a transient fashion. Simulations have predicted unstable behaviour successfully in both static mixers and stirred tanks (Paul *et al.*, 2004). This method has proved to be a powerful tool as described in Derksen (2003), Hartmann *et al.* (2004, 2006) and Yeoh *et al.* (2004). A detailed survey of the different numerical methods and results for the calculation of turbulent flows for single phase and multiphase problems can be found in Sommerfeld and Decker (2004). The recent review by Van den Akker (2006) gives further details and references on the LES method, including the lattice-Boltzmann solution techniques, for more advanced CFD approaches.

Multiphase simulations are highly computationally intensive because there are roughly twice as many equations to be solved as for a single phase simulation and the convergence is slowed due to the complexity of the multiphase physics (Lane *et al.*, 2000). Although the long calculation time and the significant computer resources necessary still remain prohibitive, particularly for multiphase problems, numerous authors, such as Brucato *et al.* (1998), Campolo *et al.* (2003), Joshi and Ranade (2003), or more recently Javed *et al.* (2006) have made good predictions of the complete flow field in unsteady conditions using the sliding-mesh (SM) approach.

Regarding these transient simulations, they are usually performed to predict a time-dependant flow but the start-up or the stopping phase of the agitator is usually omitted. The only computational study we could find that uses a non constant agitator speed was that of Smith (1997) who developed a fluid dynamics code for predicting the transient mixing after the start-up phase of the agitator in an unbaffled agitated vessel. A quasi-three dimensional single phase model, used with the $k-\varepsilon$ turbulence model and Lagrangian tracer particles as an indicator of the mixing behaviour, allowed prediction of the resuspension of a slurry after the start of the agitator. The agitator speed was linearly ramped up to 100 RPM in 5 s and the free surface at the top of the tank was assumed to be flat. In spite of a lack of experimental data for comparison, the simulations were found to agree qualitatively with mixing observations. Concerning the numerical modelling of the fluid behaviour following an agitator stopping, no results have been found in the literature.

Laboratory and pilot plant scale experiments with runaway conditions are difficult to carry out because of the hazards associated with such conditions, thus the use of computational fluid dynamics (CFD) becomes very useful in this case. The commercial CFD package ANSYS CFX 10.0 (2006) is used to develop a transient model to study the hydrodynamics during impeller slowdown. This study is devoted firstly to the modelling of the agitator stopping, applied to the case of an under-baffled stirred vessel developed for industrial applications. One of the goals of this study was to simulate, using CFD, an impeller with a decreasing speed and the associated flow in the reactor, taking into account the inertia of the fluid after the agitator has stopped and the diminution of the vortex, until the final state where there is no residual movement and a flat free surface is formed. Finally, the capability of the CFD model to predict the free surface evolution during agitator stopping was analysed via comparison with experimental data obtained by a video imaging process. The ability to predict the vortex shape during stopping is a crucial challenge to overcome to allow modelling in future studies of industrial applications, where the inhibiting agent is injected at the free surface of polymerization reactors.

CFD MODELLING

Geometry of the System Studied

Contrary to baffled or unbaffled vessels, mixing studies devoted to stirred vessels where the baffling effect is not sufficient to prevent vortex formation (called under-baffled or partially baffled vessels) have been poorly studied. The complete description of the mixing equipment used in this study and a literature review of work on unbaffled and partially baffled vessels can be found in a previous paper (Torré *et al.*, 2007). The mixing vessel modelled is composed of a bottom entering agitator derived from the Pfaudler retreat blade impeller, two beaver tail baffles suspended from the top reactor lid, a bottom curved dish and the cylindrical glass part of the vessel placed into a square water filled jacket to avoid shell curvature and refraction problems for laser measurements. The installation is presented in Figure 1 and Table 1 summarizes all of the geometrical dimensions.

The agitation speed during the stopping period is linked to the rotational inertia of the whole agitation system which includes not only the impeller and shaft but also the rotor of the electrical motor and the gear wheels of the gear reducer. The agitator system studied was constrained by a speed controller (Leroy Somer Proxidrive®) to decelerate with a linear function of time and to stop in 6.4 s. As a first approach, the experimental settings have been used in the simulations to compare CFD predictions with experimental data.

Simulation Strategy

The numerical simulations were carried out using a commercial CFD package (ANSYS CFX 10.0) to predict the flow field and the free surface shape by resolution of the Reynolds averaged continuity and Navier–Stokes equations, by using an Eulerian–Eulerian multiphase model in a fully transient manner. The fluids used were water and air at 25°C. To model the free surface deformation, an inhomogeneous model (in which a separate velocity field is determined for the gas and liquid phases) was chosen to allow phase separation. The interfacial momentum transfer between the two phases was modelled using a disperse phase model in which the liquid phase is continuous and the gas phase is dispersed. This model, characterized by the solution of an individual set of continuity and momentum equations for each phase, was coupled with a homogeneous $k-\varepsilon$ turbulence model, which assumes that the turbulent quantities are the same for the two phases. This is clearly a significant

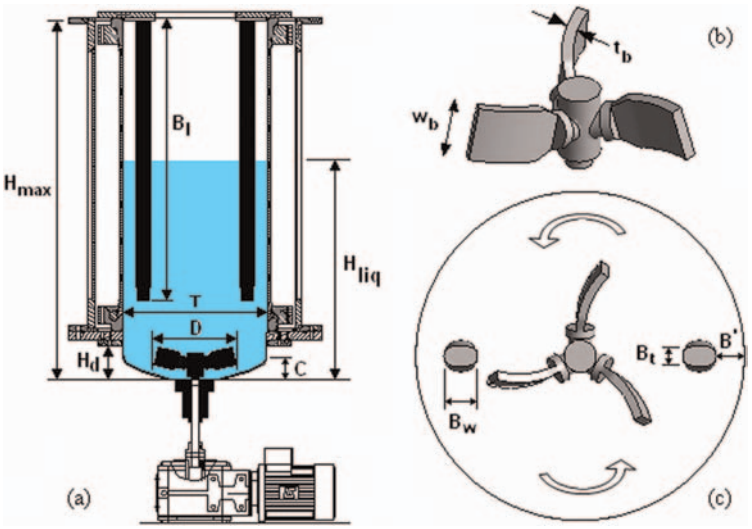

Figure 1. (a) Side view of the mixing vessel; (b) details of the agitator; (c) plan view of the mixing vessel. This figure is available in colour online via www.icheme.org/cherd

assumption, as whilst the flow will start off being fully turbulent, as the impeller slows the turbulence generated by the agitator diminishes and ultimately the flow becomes laminar. The duration of the current simulation is such that there remains significant rotational flow at the end of the calculation. This, together with the stirring effect of gas bubbles breaking away from the impeller blades as it slows down, supports the assumption of turbulent flow. The volume fractions of the phases are tracked with the condition that the volume fraction for all phases sums to unity. A constant bubble size of 3 mm and a constant drag coefficient of 0.44 have been chosen for all the simulations (Torré *et al.*, 2007).

The continuity equation, written for each phase *p*, is expressed in equation (1) by

$$\frac{\partial(\alpha_p\rho_p)}{\partial t} + \nabla\cdot(\alpha_p\rho_p\mathbf{u}_p) = 0 \tag{1}$$

where α_p is the volume fraction, ρ_p is the density and $\mathbf{u}_p$ the phase averaged velocity.

Table 1. Geometric dimensions of the agitated vessel.

	Symbol	Value
Tank diameter	T	450 mm
Maximum tank height	H_{max}	1156 mm
Bottom dish height	H_d	122.9 mm
Agitator diameter	D	260 mm
Number of agitator blades	n_b	3
Agitator blade width	w_b	58 mm
Agitator blade thickness	t_b	9 mm
Agitator retreat angle	θ	15°
Agitator clearance	C	47.2 mm
Baffles length	B_l	900 mm
Number of baffles	n_B	2
Baffle width	B_W	46 mm
Baffle thickness	B_t	27 mm
Distance baffle-reactor	B'	38.5 mm
Liquid height	H_{liq}	700 mm

The momentum equation for phase *p* is written in equation (2) as

$$\frac{\partial(\alpha_p\rho_p\mathbf{u}_p)}{\partial t} + \nabla\cdot(\alpha_p\rho_p\mathbf{u}_p\otimes\mathbf{u}_p) = -\alpha_p\nabla p + \nabla\cdot\left[\mu_p^{eff}\alpha_p\left(\nabla\mathbf{u}_p + (\nabla\mathbf{u}_p)^T\right)\right] + \alpha_p\rho_p\mathbf{g} + \mathbf{M}_{ip} \tag{2}$$

where **g** is the acceleration due to gravity and the interfacial forces acting on each phase are represented by the term $\mathbf{M}_{ip}$.

μ_p^{eff} is the effective viscosity defined by

$$\mu_p^{eff} = \mu_p^{lam} + \mu_p^{turb} \text{ with } \mu_p^{turb} = \rho_p C_\mu \frac{k^2}{\varepsilon} \text{ and } C_\mu = 0.09$$

The interfacial force term, reduced to the total drag exerted on the continuous phase on a per unit volume basis, is given by equation (3)

$$\mathbf{M}_{ip} = \mathbf{M}_{gl} = \frac{3}{4}\frac{\alpha_g\rho_l}{d_b}C_D|\mathbf{u}_g - \mathbf{u}_l|(\mathbf{u}_g - \mathbf{u}_l) \tag{3}$$

where C_D is the drag coefficient and d_b is an assumed bubble size. Note that no non-drag forces, such as turbulent diffusion, were included as our previous work showed that the simplified model presented here could capture the free surface geometry to within the experimental accuracy (Torré, *et al.*, 2007).

The values of k and ε come directly from the partial differential transport equations for the turbulent kinetic energy and the turbulence dissipation rate, which are expressed in equations (4) and (5), respectively:

$$\frac{\partial(\rho_m k)}{\partial t} + \nabla\cdot(\rho_m\mathbf{u}_m k) = \nabla\cdot\left[\left(\mu_m^{lam} + \frac{\mu_m^{turb}}{\sigma_k}\right)\nabla k\right] + P - \rho_m\varepsilon \tag{4}$$

$$\frac{\partial(\rho_m\varepsilon)}{\partial t} + \nabla\cdot(\rho_m\mathbf{u}_m\varepsilon) = \nabla\cdot\left[\left(\mu_m^{lam} + \frac{\mu_m^{turb}}{\sigma_\varepsilon}\right)\nabla\varepsilon\right] + \frac{\varepsilon}{k}(C_{\varepsilon1}P - C_{\varepsilon2}\rho_m\varepsilon) \tag{5}$$

with $\rho_m = \alpha_g\rho_g + \alpha_l\rho_l$, $\mu_m^j = \alpha_g\mu_g^j + \alpha_l\mu_l^j$ (j = lam or turb), $\mathbf{u_m} = \frac{\alpha_g\rho_g\mathbf{u_g}+\alpha_l\rho_l\mathbf{u_l}}{\rho_m}$ and $C_{\varepsilon 1}$, $C_{\varepsilon 2}$, σ_k and σ_ε are the $k-\varepsilon$ turbulence model constants equal to 1.44, 1.92, 1.0 and 1.3, respectively.

The turbulence production due to shear is given in equation (6):

$$P = \mu_m^{turb}\nabla\mathbf{u}_m \cdot \left(\nabla\mathbf{u}_m + (\nabla\mathbf{u}_m)^T\right) - \frac{2}{3}\nabla\cdot\mathbf{u}_m \times \left(3\mu_m^{turb}\nabla\cdot\mathbf{u_m} + \rho_m k\right) \quad (6)$$

During the impeller stopping phase, the flow characteristics are highly time dependent. This time dependence has been treated using the transient rotor-stator model available in ANSYS CFX 10.0, that takes the transient impeller movement into account via a SM approach. To predict the true transient interaction between a stator and a rotor passage, a sliding interface is used to allow a smooth rotation between components allowing the interface position to be updated at each time step, as the relative position of the meshes on each side of the interface is changed. This model is robust and yields high accuracy predictions of loading but the principle disadvantage of this method is that the computer resources required are large, in terms of simulation time, disk space and quantitative post processing of the data (ANSYS-CFX 10.0 *User's Guide*, 2006).

The no slip condition was applied at all solid/liquid interfaces. At the top of the vessel, a free-slip condition was set, but as the vessel lid was well removed from the region of interest this played no role in the simulation results. This last condition prevents any flow through the surface and the normal gradients for all other quantities have been set to zero. A maximum number of 15 coefficient loops per time step was adequate to resolve the strong non-linearities present in the multiphase flow equations. The transient simulations were started from a converged steady state result run at the same impeller rotation speed (275 rpm) using a multiple reference frame approach. Both simulations assumed an initial liquid height of 700 mm with 100 mm of gas above it.

The transient scheme allows modelling of the deceleration phase of the agitator by defining an impeller speed as a decreasing function of time. The impeller speed was modelled in a first approach by the linear function $N(t)$ which varied from $N_m = 275$ rpm to 0 rpm, as expressed in equation (7), in agreement with the decreasing speed function measured on the pilot reactor.

$$\begin{cases} N(t) = N_m \text{ for } t_0 \le t < t_1 \\ N(t) = \frac{N_m}{t_2 - t_1}(t_2 - t) \text{ for } t_1 \le t < t_2 \\ N(t) = 0 \text{ for } t_2 \le t < t_f \end{cases} \quad (7)$$

with t_o the initial time, t_1 and t_2 respectively the beginning and the end of the agitator stopping phase and t_f the final time, when the simulation is stopped.

The time step has been set to ensure a constant angle rotation of 2° per time step. This small rotation angle was found to give good convergence in less than 15 coefficient loops per timestep. As the impeller rotation speed is decreasing while the agitator is stopping, the time step has been modified to give a constant rotation angle of 2° by a time step function depending on the rotation speed as expressed in equation (8), which gives a maximum time step of 0.01 s.

$$\text{Time step} = \frac{1}{\text{Max}(3N,\ 100)} \quad (8)$$

An unstructured grid composed of 208 000 nodes was used in the transient simulations. The density of cells was optimized by sensitivity studies to be fine enough to capture the flow without being excessive (Torré *et al.*, 2007). Inflation meshing was used at all walls to ensure boundary layers are captured correctly. Figure 2 shows the computational grid

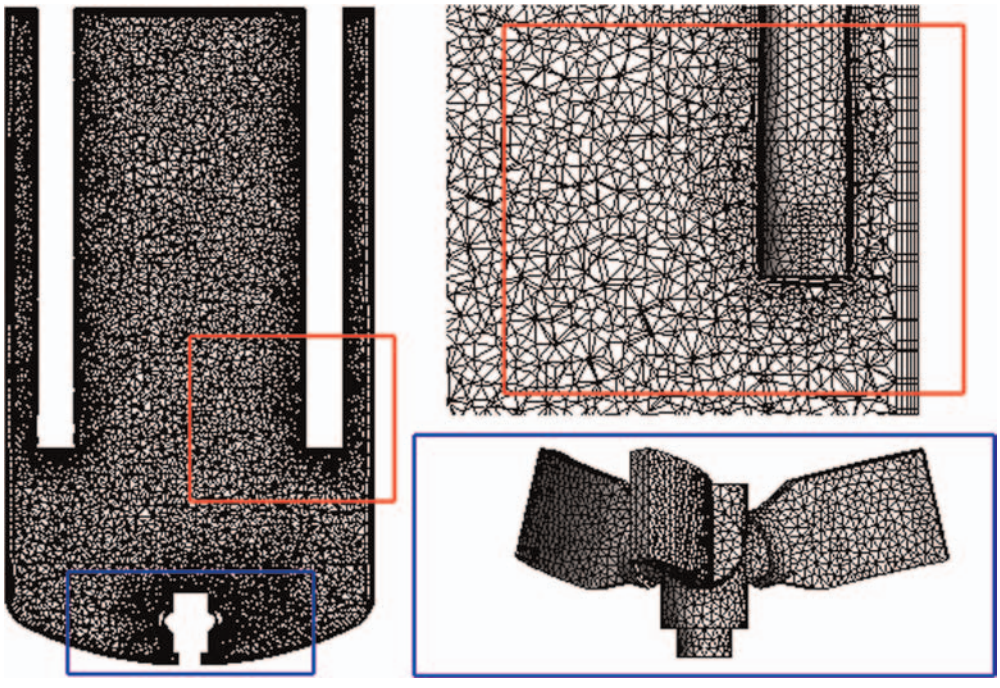

Figure 2. Details of the computational grid used in the simulation. This figure is available in colour online via www.icheme.org/cherd

,

resolution, the inflation mesh at the walls and the surface mesh on the agitator and baffles. The rotating part of the vessel was set to be the bottom dish, which includes the agitator. A second order bounded scheme was used for the convective terms in the momentum and volume fraction equations and a first order upwind scheme was used for the turbulence equations. Similarly, the transient terms were represented via a second order Euler scheme for the momentum and volume fraction equations and a first order scheme for the turbulence equations. The convergence criterion adopted for the simulation at each time step is based on the rms (root mean square) normalized values of the equations residuals. The convergence at each time step was such that the residuals for the mass, momentum and turbulence equations were below 10^{-4} and that for the volume fraction equations was below 10^{-3}. The simulation was carried out on a dual-processor Xeon 2.8 GHz computer with 2 Gbytes RAM and required 68 days of CPU time.

EXPERIMENTAL FREE SURFACE CAPTURE

The free surface shape which develops in the vessel studied is highly unsteady, so an instantaneous picture of the vortex cannot give a correct description of the free surface boundaries except in the case where the free surface is flat. The development of an experimental method of free surface capture required an imaging process technique based on a superimposition of images. When the vortex is formed and more generally when air bubbles are dispersed in water, the gas/liquid interface provides a dark area which contrasts against the transparent water medium. These contrasted areas were used to fix the boundaries of the free surface by superimposition of instantaneous pictures. When a sufficient number of pictures were superimposed, the free surface contour was highlighted. As detailed in a previous paper (Torré *et al.*, 2007), the same imaging process was successfully used to capture the free surface shapes obtained at constant rotation speeds varying from 200 rpm to 350 rpm.

The acquisition of numerous images is relatively easy for the case of constant rotation speed, but this experimental strategy is more complex to carry out during the stopping period of the agitator. For the case of non-constant agitator rotation speed, the method requires superimposing images obtained exactly at the same time during the stopping sequence. Due to the complexity of the acquisition and image post processing, only sixty experiments were made. The camera used was a high resolution CMOS camera (HCC-1000 model from VDS Vosskühler) monitored by the NV1000 software from New Vision Technologies. The camera was located 1110 mm away from and normal to the vessel jacket sidewall, and was equipped with a telephoto lens Nikon—Nikkor 50 mm/1.2. The frame rate, exposure time and total recording time were 10 frames s^{-1}, 2.2 ms and 10 s, respectively and the image resolution was 1024×1024 pixels^2. These settings remained fixed for all the captures.

The agitator speed was set at the initial speed of 275 rpm. The agitator stopping order was manually given to the speed controller at the same time the video camera was started. Ten seconds of recording time was sufficient to capture the complete evolution of the free surface from the initial state to a final flat state obtained after the agitator has completely stopped. For the 60 videos recorded, each was decomposed in 100 frames and only the frames which correspond to the times 0, 1, 2, 3, 4, 5, 6 and 7 s were kept. The frames correspond to the times marked as experimental points on Figure 3, were superimposed to give averaged pictures made by superimposition of 60 frames. This number of frames was sufficient to capture the free surface evolution during agitator stopping.

RESULTS AND DISCUSSION

The transient simulation was run with the following parameters: $t_o = -0.5$ s, $t_1 = 0$ s, $t_2 = 6.4$ s and $t_f = 9.5$ s, with an impeller rotation speed decreasing from 275 to 0 rpm. The negative value of t_o represents the fact that the simulation has been run with a transient scheme with a constant rotation speed of 275 rpm during 0.5 s after initialization with a steady state result and before starting the stopping phase at t_1. This allows the simulation to settle down in transient mode before the ramp is applied. Figure 3 shows the linear ramp of deceleration of the agitator speed and the time-step versus time.

Analysis of the Free Surface Dynamics

Figure 4 presents the numerical prediction of the free surface shape from 0 to 9.5 s. In the previous study (Torré *et al.*, 2007), a multiple reference frame (MRF) approach and steady state assumption were assumed. The numerical predictions were also compared with experimental data with very good agreement obtained by considering an isosurface of water volume fraction equal to 0.9 for the air/water interface to represent the free surface. The same volume fraction threshold was used here.

The agitator stopping phase is represented by Figure 4(a)–(n) and the inertial period which follows the complete stopping of the agitator is shown in Figure 4(o) and (p). The baffle effect provided by the two beaver tail baffles is not sufficient to prevent the highly swirling fluid movement, with a particularly unstable and deep vortex being created at a rotation speed of 275 rpm. The vortex shape shown in Figure 4(a) is characteristic of the under-baffled agitated

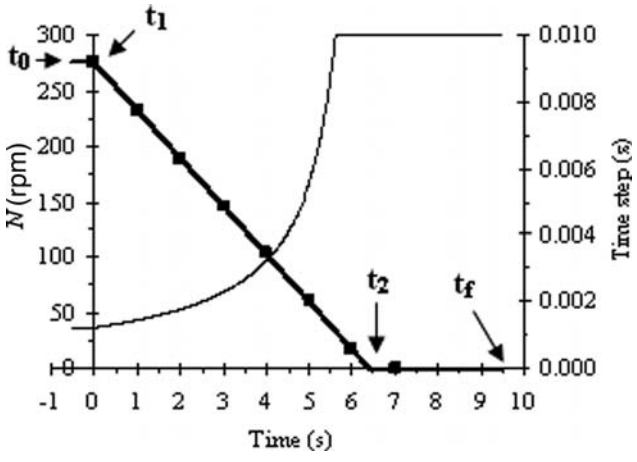

Figure 3. Agitator speed (bold line) and time-step (normal line) used in the simulations for modelling the agitator stopping. (■): experimental points for the free surface shape comparison.

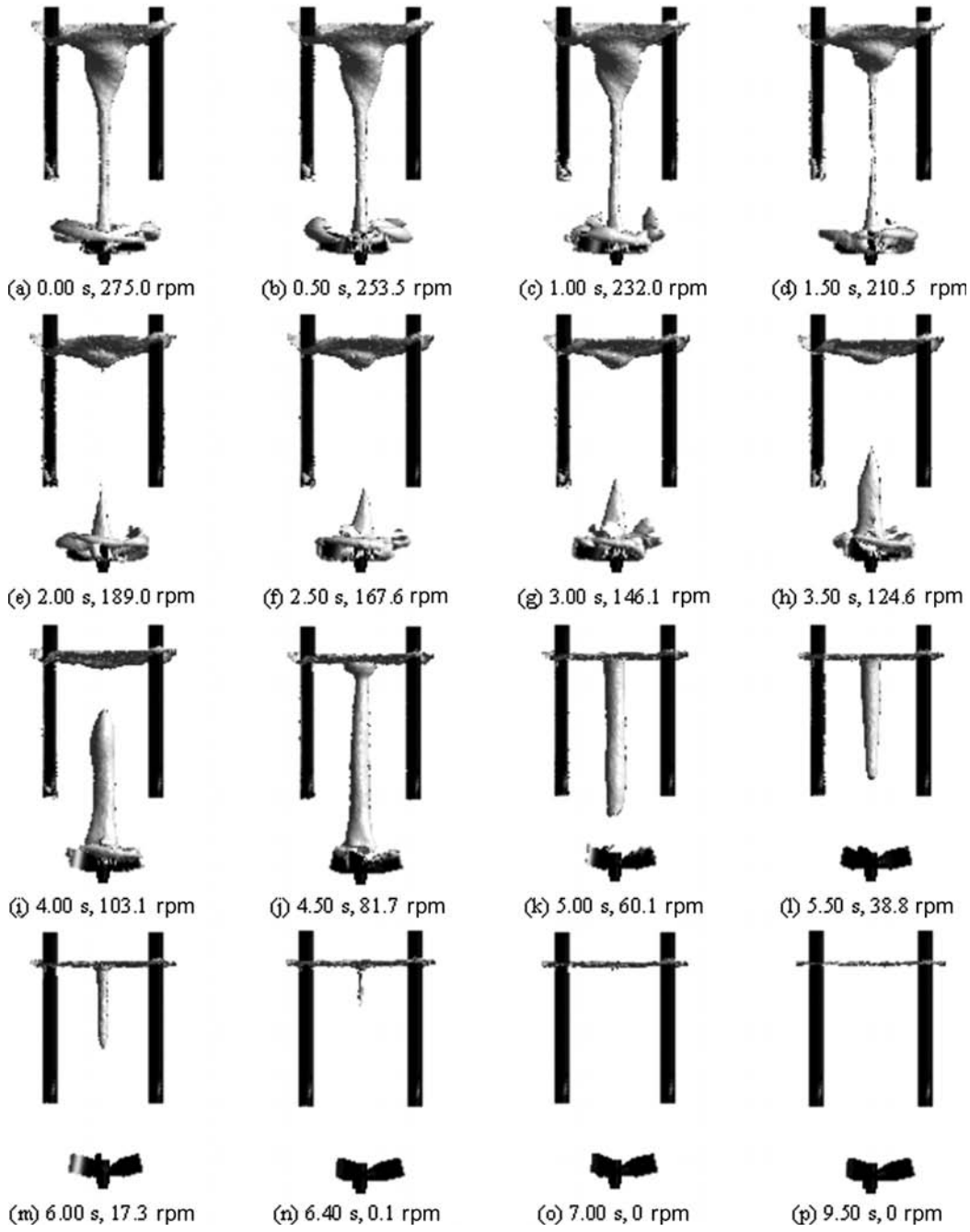

Figure 4. Evolution of the free surface during impeller slowdown and stopping (simulation time from the start of the impeller slowdown, impeller rotation speed).

vessel used in this study. The same vortex shape was predicted numerically in a previous paper (Torré *et al.*, 2007) for different impeller rotation speeds using a steady-state approach. At the bottom of the central vortex bulb, the simulation predicts a column of gas linking the vortex core to the agitator. This gas aspiration is hypothesized to be one of the causes responsible for the high gas dispersion observed experimentally at this rotation speed.

The depth of the vortex core and the diameter of the gas column decrease rapidly. It is observed that 1.5 s after stopping the impeller [Figure 4(d)] that the gas column breaks. Thus, the initial continuous region of gas separates into two regions: one comprising the vortex core and the top vessel part and one located close to the impeller. The free surface becomes flat first and then the gas located in the impeller region rises before the impeller stops completely. The free surface becomes flat roughly 2 s before the agitator stops completely (6.4 s), as shown in the Figure 4(j). As shown in Figure 4(o) and (p), the free surface remains flat during the inertial period after the agitator stops.

It can be assumed that the air bubbles in the impeller region are trapped due to low pressure in the regions of high turbulence and the vortices created by the impeller and that the gas rises when the buoyancy force becomes

dominant. This gas rise phenomenon cannot be observed in a steady state simulation because the high gas volume fraction in the impeller region observed with a low rotation speed [as shown in Fig. 4(i) with 103.1 rpm] is linked to the transient evolution history. Such a transient simulation allows the study of the hydrodynamics during the agitator stopping phase.

Flow Patterns and Velocity Profile Analysis

Figure 5 presents the liquid and gas velocities on the vertical baffle plane for two simulation times at the same relative location of the agitator blades. As shown in Figure 5, the rotation speed magnitude has a significant effect on the velocity patterns which develop in the vessel. Two circulation loops are clearly visible in Figure 5(a) for high rotation speed but only one remains at lower speed [Figure 5(b)]. At the beginning of the agitator stopping phase, the rotation speed is sufficient to maintain two circulation loops below the baffles during a complete rotation (360°) of the agitator, as shown in Figure 5(a). In contrast, the circulation loops are alternatively formed below each baffle during one 360° agitator rotation during the stopping phase. This observation confirms the high unsteadiness of the time dependant phenomena observed during this agitator stopping phase. Positive values of the axial velocity of the liquid surrounding the central gas zone are observed in Figure 5(b) due to the entrainment of the liquid by the rising gas. The distributions of liquid volume which is associated with a particular liquid speed range have been determined during the transient simulation, the liquid speed being defined as $U_{ijk} = (u^2 + v^2 + w^2)^{0.5}$ with u, v, w being the Cartesian components of the liquid velocity. The liquid speed normalized by the tip speed is denoted U^*_{ijk} and defined as U_{ijk}/U_{tip}, with $U_{tip} = \pi ND$. For different simulation times, a curve fitted to the liquid speed histogram and the liquid speed distributions normalized with the tip speed are presented in Figure 6(a) and (b), respectively.

The decrease of the agitator rotation speed during the slowing phase implies that the velocity distribution shifts from the high to the low velocity magnitudes, as can be observed in Figure 6(a). The velocity distributions normalized with the tip speed at times of 0, 3 and 4.5 s are presented in Figure 6(b). As the impeller slows down there are regions of flow that continue to rotate and these have a higher spread relative to the current tip speed, so the distributions cannot be superimposed. The history of the fluid evolution determines the instantaneous transient result by adding high velocity components that were generated earlier in time when the impeller was moving faster.

Volume-Averaged Velocity and Agitation Index

The volume-averaged velocity $\langle U \rangle$ and the agitation index I_G were first proposed by Mavros and Baudou in 1997 as a measure of the agitation quality in a stirred vessel. They evaluated the performance of various impellers using the agitation index. In the same way, Fangary *et al.* (2000) compared the effectiveness of different impellers applied with a non-Newtonian liquid and Alliet-Gaubert *et al.* (2006) used this index coupled with CFD simulations to provide an analysis for laminar or transient-laminar single phase flow in a multi-stage stirred vessel.

The agitation index of Mavros and Baudou (1997), developed and used initially for single phase mixing experiments, can be used easily in computational studies but the original formulation had to be modified for treating our numerical

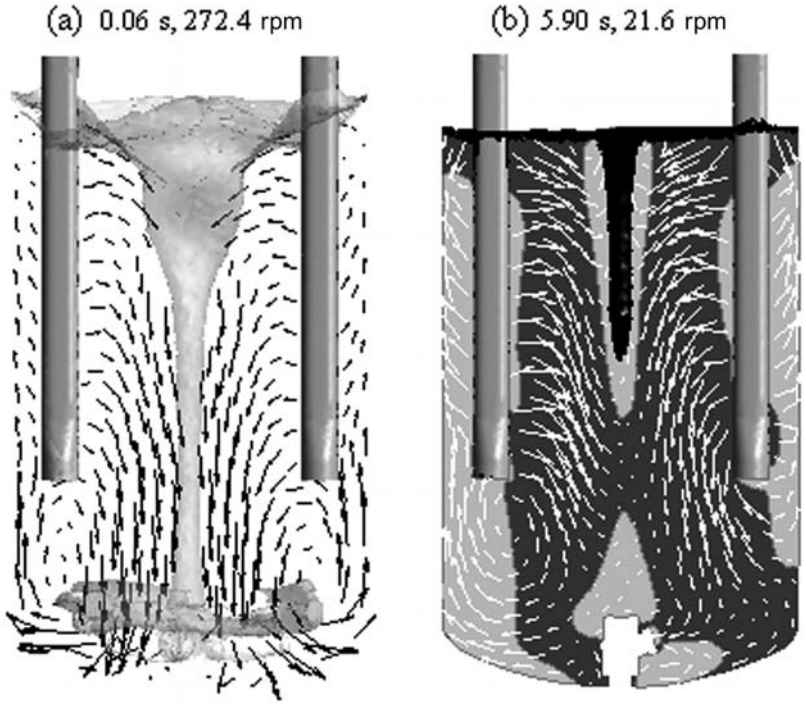

Figure 5. Radial-axial vector plots and free surface for two times from the start of the impeller slowdown; (a) black velocity vectors, free surface in light grey; (b) white velocity vectors, axial velocity contour plot with positive values in light grey and negative values in dark grey, free surface in black.

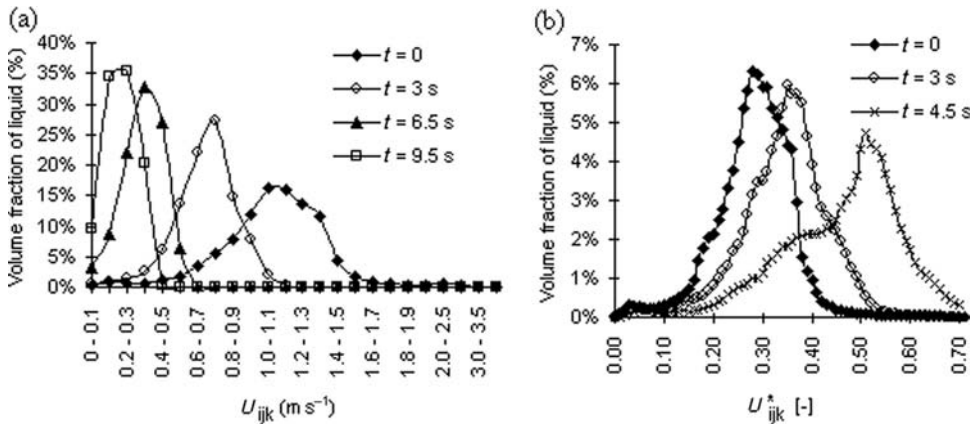

Figure 6. The distribution of liquid volumes associated with liquid velocity ranges for different simulation times; (a) volume fraction of liquid versus liquid speed, (b) volume fraction of liquid versus liquid speed normalized by the tip speed.

multiphase problem. To define the volume-averaged velocity $\langle U \rangle$ expressed in equation (9), it is postulated that each velocity U_{ijk} correspond to a volume of liquid V_{ijk}, which is related to the vessel dimension and the grid point coordinate i, j, k. To take in account the changing zones of liquid and gas resulting from the flattening of the free surface during the agitator stopping phase, the speed U_{ijk} calculated in each cell must be filtered by a function depending on the liquid volume fraction. This function, denoted $f(x)$ and defined in equation (10), allows consideration of only the cells where the liquid volume fraction $\alpha_{l,ijk}$ is above the liquid volume fraction threshold ($\alpha_l^t = 0.9$) used to define the free surface.

$$\langle U \rangle = \frac{\sum_i \sum_j \sum_k U_{ijk} V_{ijk} f(\alpha_{l,ijk})}{\sum_i \sum_j \sum_k V_{ijk} f(\alpha_{l,ijk})} \tag{9}$$

with the liquid speed U_{ijk} expressed as $U_{ijk} = (u^2 + v^2 + w^2)^{0.5}$

$$f(\alpha_{l,ijk}) = H(\alpha_{l,ijk} - \alpha_l^t) \tag{10}$$

with $\alpha_l^t = 0.9$ and where $H(x)$ is the Heaviside function (step function).

The original formulation of the agitation index, I_G, was also modified. Mavros and Baudou (1997) defined this index as the ratio of the volume-averaged velocity $\langle U \rangle$ and the agitator tip speed U_{tip}. In the case studied here, the tip velocity cannot be used as the denominator as it becomes zero when the agitator stops. Thus, the mixing quality is compared through a percentage giving the ratio of the liquid volume-averaged velocity between the initial and the final states. The modified agitation index is expressed in equation (11).

$$I_G = 100 \frac{\langle U \rangle}{\langle U_O \rangle} \tag{11}$$

The agitation index has been calculated during the agitator stopping phase and is plotted against time in Figure 7. In the same figure, the dashed line shows the theoretical lower limit of the agitation index calculated for the linear agitation speed decreasing function used in this study. The gap between the symbols and the dashed line is due to the impact of the fluid inertia during the stopping phase. This inertial effect was already shown in Figure 6(b) and discussed earlier in the paper. This agitation index analysis could be very useful as an integral quantity to describe the transient process when the agitator slows down. Particularly, it can be used to investigate the influence of different sets of parameters, to clarify the impact of the initial conditions on the dynamics of the free surface and to quantify the mixing quality during the stopping phase. Unfortunately, we have not yet been able to perform multiple simulations to test this due to the very long calculation times required.

CFD Predictions Versus Experimental Data

The comparison of the numerical predictions and experimental free surface profiles are presented in Figure 8. The numerical results represent the projection of the isosurface of water volume fraction equal to 0.9 onto the vertical baffle plane. This value has proved to give good agreement at 275 rpm with experimental averaged pictures made by superimposition of 300 frames (Torré *et al.*, 2007). The high value of 0.9 of the volume fraction threshold was attributed to the presence of the dynamical equilibrium zone of intense gas/liquid exchanges which occurs around the free surface. The experimental method appeared to be very sensitive to the gas dispersed in the vessel and particularly if the number of frames superimposed is less than 200. In this case, a dark area can be observed on the final averaged picture

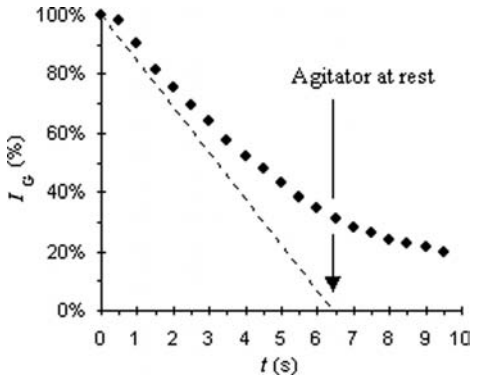

Figure 7. The agitation index versus time during the agitator stopping phase and the inertial period.

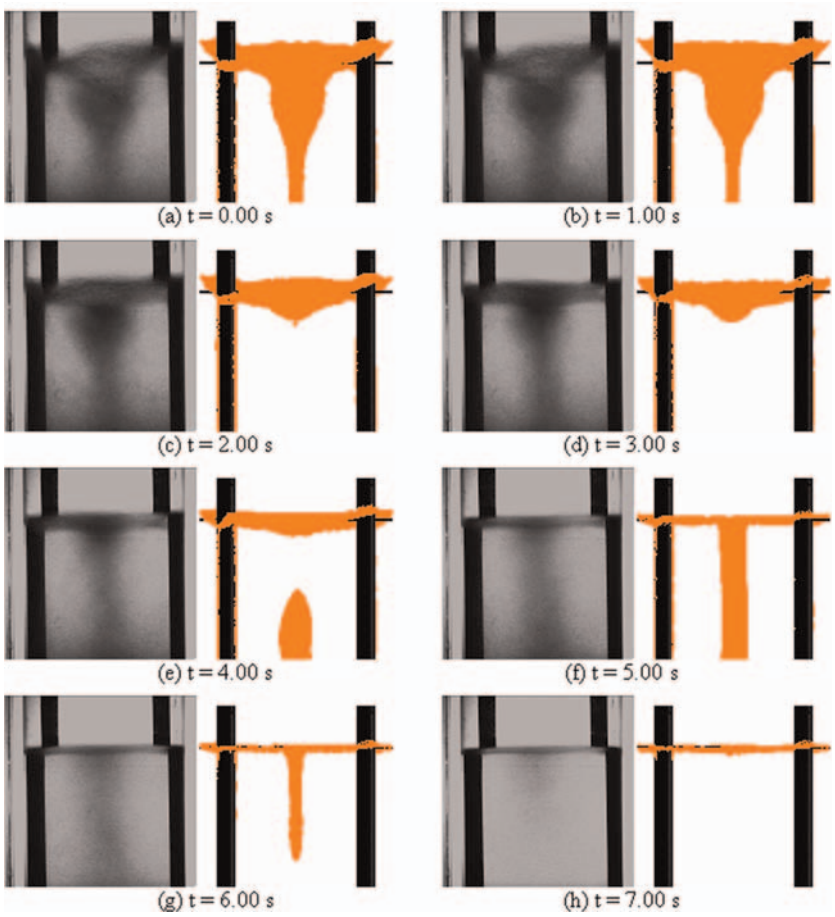

Figure 8. Comparison between experimental data and numerical predictions of the free surface shape profile during agitator stopping. For each time: left: experimental; right: numerical. This figure is available in colour online via www.icheme.org/cherd

even if a small percentage of gas is present. The fact that only 60 frames have been superimposed to obtain Figure 8 yields a wide area of gas/liquid exchange near the free surface boundaries on the average picture. It may explain why the experimental vortex appears larger than the numerical prediction. Nevertheless, this uncommon vortex shape obtained experimentally at 275 rpm, which is so distinctive with its central bulb, is in agreement with the numerical result. The liquid elevation, the bulb and the gas column at the vortex bottom are well predicted. In contrast, the gas dispersion visible in the bottom experimental picture of Figure 8(a) is not obtained numerically. This is because the current simulation does not model the bubble production process of shear-induced stripping at the gas–liquid interface.

As shown in Figure 8(c) and (d), the model predicts separated gas regions located in the top vessel and in the agitator area [also visible in Figure 4(e) and (g)], with a significant vortex depth decrease, and a free surface which has flattened compared with the initial state. Experimentally, the averaged picture at these times reveals a free surface bulb shape close to the initial state and no distinct gas segregation was observed. The free surface flattens in agreement with numerical predictions. When the free surface becomes almost flat, good agreement between the experimental data and numerical predictions is observed, as shown in Figure 8(e)–(h).

We note that the predicted free surface evolution could be highly dependent on the time at which the agitator speed is reduced. In a recent CFD study (Torré *et al.*, 2006), the simulation of the same vessel with only water and a flat free surface at 100 rpm during 35 agitator revolutions revealed very complex flow and vortical structures associated with low frequency instabilities linked to the under-baffled configuration. Thus, running in transient mode for several agitator rotations at constant speed and then stopping the agitator may lead to different free surface shape profiles depending on the flow structure just before the point of stopping. In the 60 experiments carried out, it was clearly visible that the free surface shape profile can be different from one run to another. Averaging the free surface profiles appears to be a good way of avoiding the high dependence of the initial conditions. Thus, the discrepancies observed between experimental data and numerical predictions during agitator stopping are highly linked to the initial state. The numerical shape evolution presented in this study has to be considered as one of the possible solutions amongst all of the various possibilities.

This analysis shows that the discrepancies that exist between the modelling and the experimental data could also come from either the modelling hypothesis or from the experimental strategy of free surface capture. The complex physical phenomena that develop in the dynamical equilibrium zone of intense gas/liquid exchanges cannot be fully taken into account in the modelling. Inclusion of only drag forces may not represent fully the physics of the problem, particularly when the global system is highly unsteady, as

in the under-baffled case studied here. The interfacial forces acting on the gas bubbles should also contain virtual mass, lift forces, turbulent dispersion, and so on but the modelling of such forces remains a major challenge. Nevertheless, the global features of the free surface shape evolution during the stopping phase is well predicted. The initial and final states and the global dynamics of the free surface flattening phenomenon observed numerically are in good agreement with physical considerations and experimental data. In addition, the numerical prediction of gas disengagement located in the impeller region is observed experimentally during the stopping phase. Thus, although the model was used with simplified physics, the inhomogeneous approach appears a good solution for modelling free surface profiles and transient hydrodynamics, even in conditions with gas disengagement and decreasing agitator speed.

CONCLUSION

CFD simulations, using a gas/liquid inhomogeneous model, coupled with a homogenous turbulence model in a full transient scheme, have been run to predict the vortex shape and the flow field in an under-baffled agitated vessel during stopping. Qualitative and quantitative numerical and experimental data have been extracted to visualize the dynamics of the free surface and to describe the time dependant phenomenon occurring during the impeller slowing phase, including the inertial period after the agitator has completely stopped. The CFD results obtained are in accord with physical considerations and the free surface shape evolution tendency predicted numerically is in good agreement with experimental data. The study of the hydrodynamics of the stirred tank during the stopping phase, together with an estimation of the mixing behaviour based on the agitation index during the transient process, has revealed that the history of the fluid evolution and the effect of the fluid inertia during the impeller slowing phase determine the instantaneous results. Therefore the flow field at any given time during the stopping phase cannot be determined via a classical steady-state approach. Modelling free surface profiles by using a gas/liquid inhomogeneous approach appears a good solution even with simplified physics, as shown by the results obtained previously with an MRF approach and a steady state assumption (Torré *et al.*, 2007) and here in a full transient manner. Nevertheless, the inertial period has to be considered carefully and the criterion for switching between turbulent and laminar flow has to be investigated in depth if the simulations are to be continued to the point at which the fluid comes to rest.

Future work will consider the effect of using the scale-adaptive simulation (SAS) turbulence model (Menter and Egorov, 2005; Menter *et al.*, 2003) instead of the $k-\varepsilon$ model. Active research work is currently devoted to the modelling of liquid jet injections on the free surface of this type of under-baffled stirred vessels to answer the questions of how, when and at what free surface location the stopper must be injected during an agitator stopping incident in polymerization reactors.

NOMENCLATURE

B'	distance baffle–reactor, mm
B_l	baffles length, mm
B_t	baffle thickness, mm
B_w	baffle width, mm
C	agitator clearance, mm
C_D	drag coefficient, dimensionless
$C_{\varepsilon 1}$	$k-\varepsilon$ model constant, dimensionless
$C_{\varepsilon 2}$	$k-\varepsilon$ model constant, dimensionless
C_μ	$k-\varepsilon$ model constant, dimensionless
D	agitator diameter, mm
d_b	bubble diameter, mm
$\mathbf{g}$	gravity acceleration, ms^{-2}
H_d	bottom dish height, mm
H_{liq}	liquid height, mm
H_{max}	maximum tank height, mm
I_G	agitation index, %
k	turbulent kinetic energy, $m^2\ s^{-2}$
$\mathbf{M}_{gl}$	drag force per unit volume, $N\ m^{-3}$
$\mathbf{M}_{ip}$	interfacial forces per unit volume, $N\ m^{-3}$
N	agitator rotation speed, rpm
N_m	initial angular velocity before agitator stopping, rpm
n_b	number of agitator blades, dimensionless
n_B	number of baffles, dimensionless
P	turbulence production, $kg\ m^{-1}\ s^{-3}$
p	pressure, Pa
T	tank diameter, mm
t	time, s
t_b	agitator blade thickness, mm
U_{ijk}	liquid speed, $m\ s^{-1}$
U^*_{ijk}	liquid speed normalized by the tip speed, dimensionless
U_{tip}	impeller tip velocity, $m\ s^{-1}$
$\langle U \rangle$	volume averaged velocity, $m\ s^{-1}$
$\langle U_o \rangle$	initial volume averaged velocity, $m\ s^{-1}$
$\mathbf{u}$	velocity, $m\ s^{-1}$
V_{ijk}	volume of liquid related the grid point coordinate i, j, k, m^3
u	Cartesian velocity component of the liquid velocity, $m\ s^{-1}$
v	Cartesian velocity component of the liquid velocity, $m\ s^{-1}$
w	Cartesian velocity component of the liquid velocity, $m\ s^{-1}$
w_b	agitator blade width, mm
x	generic variable for mathematical function definitions

Greek symbols

α	volume fraction, dimensionless
ε	dissipation rate of turbulent energy per unit volume, $m^2\ s^{-3}$
μ	dynamic viscosity, $kg\ m^{-1}\ s^{-1}$
θ	agitator retreat angle, degrees
ρ	density, $kg\ m^{-3}$
σ_k	$k-\varepsilon$ model constant, dimensionless
σ_ε	$k-\varepsilon$ model constant, dimensionless

Subscripts

g	gas phase
i	interfacial
i j k	relative to the Cartesian coordinates i, j, k
l	liquid phase
m	mean
p	phase index

Superscripts

eff	effective
lam	laminar
T	matrix transposition
t	threshold
turb	turbulent

Mathematical functions

$f(x)$	filter function in the agitation index definition
$H(x)$	Heaviside function

Balasubramanian, S.G. and Louvar, J.F., 2002, Study of major accidents and lessons learned, *Proceedings of Safety Progress*, 21(3): 237–244.
Barton, J.A. and Nolan, P.F., 1989, Incidents in the chemical industry due to thermal runaway chemical reactions. Hazards X: Process safety in fine and specialty chemical plants, *Symposium series*, 115: 3–18.
Brucato, A., Ciofalo, M., Grisafi, F. and Micale, G., 1998, Numerical prediction of flow fields in baffled stirred vessels: a comparison of alternative modelling approaches, *Chem Eng Sci*, 53(21): 3653–3684.
Campolo, M., Sbrizzai, F. and Soldati, A., 2003, Time-dependent flow structures and Lagrangian mixing in Rushton-impeller baffled-tank reactor, *Chem Eng Sci*, 58(8): 1615–1629.
Dakshinamoorthy, D., Khopkar, A.R., Louvar, J.F. and Ranade, V.V., 2004, CFD simulations to study shortstopping runaway reactions in a stirred vessel, *Journal of Loss Prevention in the Process Industries*, 17: 355–364.
Dakshinamoorthy, D., Khopkar, A.R., Louvar, J.F. and Ranade, V.V., 2006, CFD simulation of shortstopping runaway reactions in vessels agitated with impellers and jets, *Journal of Loss Prevention in the Process Industries*, 6: 570–581.
Derksen, J.J., 2003, Numerical simulation of solids suspension in a stirred tank, *AIChE J*, 49: 2700–2714.
Fangary, Y.S., Barigou, M., Seville, J.P.K. and Parker, D.J., 2000, Fluid trajectories in a stirred vessel of non-newtonian liquid using positron emission particle tracking, *Chem Eng Sci*, 55(24): 5969–5979.
Hartmann, H., Derksen, J.J., Montavon, C., Pearson, J., Hamill I.S. and Van den Akker, H.E.A., 2004, Assessment of large eddy and RANS stirred tank simulations by means of LDA, *Chem Eng Sci*, 59(12): 2419–2432.
Hartmann, H., Derksen, J.J. and Van den Akker, H.E.A., 2006, Numerical simulation of a dissolution process in a stirred tank reactor, *Chem Eng Sci*, 61: 3025–3032.
Hristov, H.V. and Mann, R., 2002, Fluid mixing and the safe quenching of runaway reaction in a stirred autoclave, *Trans IChemE*, 80(A): 872–879.
Javed, K.H., Mahmud, T. and Zhu, J.M., 2006, Numerical simulation of turbulent batch mixing in a vessel agitated by a Rushton turbine, *Chem Eng Process*, 45(2): 99–112.
Joshi, J.B. and Ranade, V.V., 2003, Computational fluid dynamics for designing process equipment: expectations, current status, and path forward, *Ind Eng Chem Res*, 42: 1115–1128.
Kammel, U., Schlüter, S., Steiff, A. and Weinspach, P.M., 1996, Control of runaway polymerization reactions by injection of inhibiting agents—A contribution to the safety of chemical reactors, *Chem Eng Sci*, 51(10): 2253–2259.
Lane, G.L., Schwarz, M.P. and Evans, G.M., 2000, Comparison of CFD methods for modelling of stirred tanks, *Proc 10th Eur Conf on Mixing*, Delft, 2–5 July, 273–280.
Mavros, P. and Baudou, C., 1997, Quantification of the performance of agitators in stirred vessels: definition and use of an agitator index, *Trans IChemE*, 75(A): 737–745.
Menter, F.R. and Egorov, Y., 2005, A scale-adaptive simulation model using two equation models, AIAA paper 2005–1095.
Menter, F.R., Kuntz, M. and Bender, R., 2003, A scale-adaptive simulation model for turbulent flow prediction, AIAA paper 2003–0767.
Paul, E.L., Atiemo-Obeng, V.A. and Kresta, S.M., 2004, *Handbook of Industrial Mixing: Science and Practice* (Wiley, Hoboken, New Jersey, USA).
Sbrizzai, F., Lavezzo, V., Verzicco, R., Campolo, M. and Soldati. A., 2006, Direct numerical simulation of turbulent particle dispersion in an unbaffled stirred-tank reactor, *Chem Eng Sci*, 61(9): 2843–2851.
Smith, F.G., 1997, A model of transient mixing in a stirred tank, *Chem Eng Sci*, 52(9): 1459–1478.
Sommerfeld, M. and Decker, S., 2004, State of the art and future trends in CFD simulation of stirred vessel hydrodynamics, *Chem Eng Technol*, 27: 215–224.
Torré, J.P., Fletcher, D.F., Lasuye, T. and Xuereb, C., 2006, CFD modelling of partially baffled agitated vessels with free surfaces, *Proc Fifth International Conference on CFD in the Process Industries*, CSIRO, 13–15 December, Melbourne, Australia.
Torré, J.P., Fletcher, D.F., Lasuye, T. and Xuereb, C., 2007, An experimental and computational study of the vortex shape in a partially baffled agitated vessel, *Chem Eng Sci*, 62: 1915–1926.
Van den Akker, H.E.A., 2006, The details of the turbulent mixing process and their simulation, *Advances in Chemical Engineering*, V31: 151–229.
Verzicco, R., Fatica, M., Iaccarino, G. and Orlandi P., 2004, Flow in an impeller-stirred tank using an immersed-boundary method, *AIChE J*, 50(6): 1109–1118.
Yeoh, S.L., Papadakis, G., Lee, K.C. and Yianneskis, M., 2004, Large eddy simulation of turbulent flow in a Rushton impeller stirred reactor with sliding-deforming mesh methodology, *Chem Eng Technol*, 27: 257–263.

ACKNOWLEDGEMENTS

Tessenderlo Group and ANRT are acknowledged for financial support. The authors are grateful to Alain Muller and Robinson Lhuillier for their help, and to the technical staff of the Chemical Engineering Laboratory of Toulouse.

The manuscript was received 29 September 2006 and accepted for publication after revision 21 March 2007.